Contrasting terrestrial carbon cycle responses to the 1997/98 and 2015/16 extreme El Niño events

Jun Wang[1,2], Ning Zeng[2,3], Meirong Wang[4], Fei Jiang[1], Hengmao Wang[1], and Ziqiang Jiang[1]

[1]International Institute for Earth System Science, Nanjing University, Nanjing, China

[2] State Key Laboratory of Numerical Modelling for Atmospheric Sciences and Geophysical Fluid Dynamics, Institute of Atmospheric Physics, Beijing, China

[3]Department of Atmospheric and Oceanic Science and Earth System Science Interdisciplinary Center, University of Maryland, College Park, Maryland, USA

[4]Joint Center for Data Assimilation Research and Applications/Key Laboratory of Meteorological Disaster of Ministry of Education, Nanjing University of Information Science & Technology, Nanjing, China

Correspondence to: J. Wang (wangjun@nju.edu.cn)

Abstract

Large interannual atmospheric CO_2 variability is dominated by the response of the terrestrial biosphere to El Niño–Southern Oscillation (ENSO). However, the behavior of terrestrial ecosystems differs during different El Niños in terms of patterns and biological processes. Here, we comprehensively compare two extreme El Niños (2015/16 and 1997/98) in the context of a multi-event 'composite' El Niño. We find large differences in the terrestrial carbon cycle responses, even though the two events were of similar magnitude.

More specifically, we find that the global-scale land–atmosphere carbon flux (F_{TA}) anomaly during the 1997/98 El Niño was 1.64 Pg C yr^{-1}, but half that quantity during the 2015/16 El Niño (at 0.73 Pg C yr^{-1}). Moreover, F_{TA} showed no obvious lagged

27 response during the 2015/16 El Niño, in contrast to that during 1997/98. Separating the

28 global flux by geographical regions, the fluxes in the tropics and extratropical northern

29 hemisphere were 1.70 and -0.05 Pg C yr^{-1} during 1997/98, respectively. During

30 2015/16, they were 1.12 and -0.52 Pg C yr^{-1}, respectively. Analysis of the mechanism

31 shows that, in the tropics, the widespread drier and warmer conditions caused a

32 decrease in gross primary productivity (GPP; -0.73 Pg C yr^{-1}) and an increase in

33 terrestrial ecosystem respiration (TER; 0.62 Pg C yr^{-1}) during the 1997/98 El Niño. In

34 contrast, anomalously wet conditions occurred in the Sahel and East Africa during

35 2015/16, which caused an increase in GPP, compensating for its reduction in other

36 tropical regions. As a result, the total 2015/16 tropical GPP and TER anomalies were

37 -0.03 and 0.95 Pg C yr^{-1}. GPP dominance during 1997/98 and TER dominance during

38 2015/16 accounted for the phase difference in their F_{TA}. In the extratropical northern

39 hemisphere, the large difference occurred because temperatures over Eurasia were

40 warmer during the 2015/16, as compared with the cooling seen during the 1997/98 and

41 the composite El Niño. These warmer conditions enhanced GPP and TER over Eurasia

42 during the 2015/16 El Niño, while these fluxes were suppressed during 1997/98. The

43 total extratropical northern hemisphere GPP and TER anomalies were 0.63 and 0.55 Pg

44 C yr^{-1} during1997/98, and 1.90 and 1.45 Pg C yr^{-1} during 2015/16, respectively.

45 Additionally, wildfires played a less important role during the 2015/16 than during the

46 1997/98 El Niño.

47

48

49

50

51

1 Introduction

The atmospheric CO_2 growth rate has significant interannual variability, greatly influenced by the El Niño–Southern Oscillation (ENSO) (Bacastow, 1976; Keeling et al., 1995). This interannual variability primarily stems from terrestrial ecosystems (Bousquet et al., 2000; Zeng et al., 2005). There is also a general consensus that the tropical terrestrial ecosystems account for the terrestrial carbon variability (Cox et al., 2013; Peylin et al., 2013; Wang et al., 2016; Wang et al., 2013; Zeng et al., 2005). They tend to release anomalous levels of carbon flux during El Niño episodes, and take up carbon during La Niña events (Wang et al., 2016; Zeng et al., 2005). Recently, Ahlstrom et al. (2015) further suggested that ecosystems in semi-arid regions dominated the terrestrial carbon interannual variability, with a 39% contribution.

The terrestrial dominance primarily results from the drive-response mechanisms in climate variability (especially in temperature and precipitation) caused by ENSO and plant/soil physiology (Jung et al., 2017; Tian et al., 1998; Wang et al., 2016; Zeng et al., 2005). The land–atmosphere carbon flux (F_{TA} – positive sign meaning a flux into the atmosphere) can mainly be attributed to the imbalance between the gross primary productivity (GPP) and terrestrial ecosystem respiration (TER) according to $F_{TA} \cong TER - GPP + C_{fire}$, where the carbon flux from wildfires (C_{fire}) is generally much smaller than the GPP or TER. Variations in each, or all, result in the changes in F_{TA}.

Based on a dynamical global vegetation model (DGVM), Zeng et al. (2005) found that net primary productivity (NPP) contributed to almost three quarters of the tropical F_{TA} interannual variability. Multi-model simulations involved in the TRENDY project and CMIP5 have consistently suggested that NPP or GPP dominate the terrestrial carbon variability (Ahlstrom et al., 2015; Kim et al., 2016; Piao et al., 2013; Wang et al., 2016). These biological process analyses suggest that precipitation variation is the dominant

77 climate factor in controlling F_{TA} interannual variability (Ahlstrom et al., 2015; Qian et

78 al., 2008; Tian et al., 1998; Wang et al., 2016; Zeng et al., 2005). Qian et al. (2008)

79 calculated the contributions of tropical precipitation and temperature as 56% and 44%,

80 respectively, based on model sensitivity experiments. Eddy covariance network

81 observations have suggested that the interannual carbon flux variability over tropical

82 and temperate regions is controlled by precipitation, while boreal ecosystem carbon

83 fluxes are more affected by temperature and radiation (Jung et al., 2011). At the same

84 time, there is a significant positive correlation between the atmospheric CO_2 growth

85 rate and mean tropical land temperature (Anderegg et al., 2015; Cox et al., 2013; Wang

86 et al., 2013; Wang et al., 2014). Regression analysis indicates an anomaly of

87 approximately 3.5 Pg C yr^{-1} in the CO_2 growth rate with a 1°C increase in tropical land

88 temperature, whereas a weaker interannual coupling exists between the CO_2 growth

89 rate and tropical land precipitation (Wang et al., 2013). Clark et al. (2003) and Doughty

90 et al. (2008) also concluded, based on in-situ observations, that warming anomalies can

91 reduce tropical tree growth and CO_2 uptake. Therefore, considering this strong

92 emergent linear relationship, these studies (Anderegg et al., 2015; Cox et al., 2013;

93 Clark et al., 2003; Doughty et al., 2008; Wang et al., 2013; Wang et al., 2014) have

94 suggested that temperature dominates the interannual variability of the F_{TA} or CO_2

95 growth rate. To reconcile these contradictory reports, Jung et al. (2017) showed that the

96 temporal and spatial compensatory effects in water availability link the yearly global

97 F_{TA} variability to temperature. Fang et al. (2017) suggested an ENSO-phase-dependent

98 interplay between water availability and temperature in controlling the tropical

99 terrestrial carbon cycle response to climate variability.

100 Apart from these long-term time series studies on the interannual F_{TA} or CO_2 growth

101 rate variability, we should keep in mind that the terrestrial carbon cycle responds in a

unique way in terms of its strength, spatial patterns, biological processes, to every El Niño/La Niña event, because of the ENSO diversity with different spatial patterns and evolutions (Capotondi et al., 2015; Schwalm, 2011). For example, wildfires played an important role in the F_{TA} anomalies during the 1997/98 El Niño (van der Werf et al., 2004). Therefore, it is important to have clear insight into the impacts of individual ENSO events on the terrestrial carbon cycle, and this is best achieved through representative case studies. Recently, one of the three extreme El Niño events in recorded history occurred in 2015/16 (https://www.esrl.noaa.gov/psd/enso/current.html). Because of the interference of the El Chichón eruption during the extreme El Niño case in 1982/83, we chose to compare in detail the response of terrestrial ecosystems in the other two extreme El Niño events, i.e., in 1997/98 and 2015/16, in the context of a multi-event 'composite' El Niño, based on the VEGAS DGVM in its near-real-time framework and inversion datasets [Copernicus Atmosphere Monitoring Service (CAMS), Monitoring Atmospheric Composition & Climate (MACC), and CarbonTracker]. The purpose is to clarify the different responses of biological processes in these two extreme events.

The paper is organized as follows: Section 2 describes the mechanistic carbon cycle model used, its drivers, and reference datasets. Section 3 presents the results of the total terrestrial carbon flux anomalies and spatial patterns, along with their mechanisms. Finally, a discussion and concluding remarks are provided in Section 4.

2   Model, datasets and Methods

2.1 Mechanistic carbon cycle model and its drivers

We used the state-of-the-art VEGAS DGVM, version 2.4, in its near-real-time framework, to investigate the responses of terrestrial ecosystems to El Niño events.

127 VEGAS has been widely used to study the terrestrial carbon cycle on its seasonal cycle,

128 interannual variability, and long-term trends (Zeng et al., 2005; Zeng et al., 2004; Zeng

129 et al., 2014). The model has also extensively participated in international carbon

130 modelling projects, such as the Coupled Climate–Carbon Cycle Model Intercomparison

131 Project (C^4MIP; Friedlingstein et al., 2006), the TRENDY project (Sitch et al., 2015)

132 and the Multi-scale Synthesis and Terrestrial Model Intercomparison Project (MsTMIP;

133 Huntzinger et al., 2013). A detailed description of the model structure and biological

134 processes can be found in the appendix of Zeng et al. (2005). We ran VEGAS at the

135 0.5°×0.5° horizontal resolution from 1901 until the end of 2016, and focused on the

136 period from 1980 to 2016.

137 The climate fields and boundary forcings used to run VEGAS were:

138 (1) Precipitation datasets generated by combining the Climatic Research Unit (CRU)

139 Time-series (TS) Version 3.22 (University of East Anglia Climatic Research Unit et al.,

140 2014), NOAA's Precipitation Reconstruction over Land (PREC/L) (Chen et al., 2002),

141 and the NOAA–NCEP Climate Anomaly Monitoring System-Outgoing Longwave

142 Radiation Precipitation Index (CAMS-OPI) (Janowiak and Xie, 1999).

143 (2) Temperature data from the CRU TS3.22 before the year 2013, and generated by

144 combining the CRU 1981–2010 climatology and the Goddard Institute for Space

145 Studies (GISS) Surface Temperature Analysis (GISTEMP) (Hansen et al., 2010) after

146 2013.

147 (3) Downward shortwave radiation from the driver datasets in MsTMIP (Wei et al.,

148 2014) before 2010, with the value of the year 2010 repeated for subsequent years.

149 (4) The gridded cropland and pasture land use datasets integrated from the History

150 Database of the Global Environment (HYDE) (Klein Goldewijk et al., 2011) with an

151 linear extrapolation in 2016.

152

2.2 Reference datasets

We selected a series of reference datasets to compare to the VEGAS simulation. The atmospheric CO_2 concentrations were from the monthly in-situ CO_2 datasets at the Mauna Loa Observatory, Hawaii (Keeling et al., 1976). The Niño 3.4 (120°W–170°W, 5°S–5°N) sea surface temperature anomaly (SSTA) data were from the NOAA's Extended Reconstructed Sea Surface Temperature (ERSST) dataset, version 4 (Huang et al., 2015), with a three-month running average. We compared the CAMS (1980–2015) and MACC (1980–2014) inversion results (Chevallier, 2013) and the CarbonTracker2016 (2000–2015) with the CarbonTracker near-real time results from 2016 (Peters et al., 2007) with VEGAS. The F_{TA} in CarbonTracker was calculated by the sum of the posterior biospheric flux and its imposed fire emissions. The Satellite-based fire emissions were from the Global Fire Emissions Database, Version 4 (GFEDv4) from 1997 through 2014 (Randerson et al., 2015). Owing to the high correlation between the solar-induced chlorophyll fluorescence (SIF) and terrestrial GPP (Guanter et al., 2014), we selected the monthly satellite SIF from the GOME2_F version 26 from 2007 to 2016 (Joiner et al., 2012). We also compared the Enhanced Vegetation Index (EVI) from MODIS MOD13C2 (Didan, 2015) with the simulated leaf area index (LAI) anomalies.

171

2.4 Methods

To calculate the anomalies during the El Niño events, we first removed the long-term climatology in each dataset for getting rid of seasonal cycle signals. We then detrended them based on the linear regression, because the trend was mainly caused by long-term CO_2 fertilization and climate change. We used these detrended monthly anomalies to

177   investigate the impacts of El Niño events on the terrestrial carbon cycle.

178

3   Results

3.1 Total terrestrial carbon flux anomalies

181   Three extreme El Niño events (1982/83, 1997/98, and 2015/16) occurred from 1980 to

182   2016, with their maximum SSTAs above 2.0 K (Fig. 1a). An El Niño event tends to

183   anomalously increase the atmospheric CO_2 growth rate (Fig. 1b); therefore, there are

184   two significant anomalous increases in CO_2 growth rate that correspond to the 1997/98

185   and 2015/16 El Niño events, although the maximum increase in 2015/16 was slightly

186   less than that in 1997/98. Because of the diffuse light disturbance (Mercado et al., 2009)

187   of the Mount El Chichón eruption during the 1982/83 El Niño on the canonical coupling

188   between the anomalies of the CO_2 growth rate anomalies and El Niño events, we mainly

189   focused on the 1997/98 and 2015/16 El Niño events in this study. The interannual

190   variability of the atmospheric CO_2 growth rate principally originates from the terrestrial

191   ecosystems (Fig. 1c). The correlation coefficient between the CO_2 growth rate

192   anomalies and the global F_{TA} simulated by VEGAS was 0.60 ($p < 0.05$). In order to

193   evaluate the performance of the VEGAS simulation on the interannual time scale, we

194   also present CAMS, MACC and CarbonTracker inversion results. The CAMS and

195   MACC inversions were nearly the same, with a correlation coefficient of approximately

196   0.60 ($p < 0.05$) with VEGAS. From 2000 to 2016, CarbonTracker was highly correlated

197   with VEGAS ($r = 0.67$, $p < 0.05$). These high correlation coefficients between VEGAS

198   and the reference datasets indicate that VEGAS can capture the terrestrial carbon cycle

199   interannual variability well.

200   There were 10 El Niño events from 1980 to 2016, each with a different duration and

201   strength (Table 1). According to the definition of El Niño, these 10 events can be

202 categorized into two weak (with a 0.5 to 0.9 SSTA), three moderate (1.0 to 1.4), two

203 strong (1.5 to 1.9), and three very strong (≥2.0) events. During the 1997/98 El Niño,

204 the positive SSTA lasted from April 1997 to June 1998, while the positive SSTA

205 occurred in winter 2014, and extended to June 2016 in the 2015/16 El Niño (Fig. 2a).

206 However, every El Niño event always peaks in winter (November or December; Fig.

207 2a). Considering this phase-lock phenomenon in the El Niño events, we produced a

208 composite analysis (excluding 1982/83 and 1991/92, because of the diffuse radiation

209 disturbances) as the background responses of the terrestrial carbon cycle to El Niño

210 events.

211 The evolution of the global F_{TA} anomalies in VEGAS, the mean of CAMS and MACC,

212 and CarbonTraker in the composite, 1997/98, and 2015/16 El Niño events, are closely

213 consistent with the Mauna Loa CGR anomalies (Figs. 2b–d). The peaks of the F_{TA} and

214 the Mauna Loa CGR anomalies in the 1997/98 and 2015/16 El Niño events were much

215 stronger than those in the composite analysis. Importantly, there were significant

216 terrestrial lagged responses in the composite and 1997/98 El Niño events, with the peak

217 of the F_{TA} anomaly occurring from March to April in the El Niño decaying year (Figs.

218 2b and c), consistent with previous studies (Qian et al., 2008; Wang et al., 2016).

219 However, this lagged terrestrial response disappeared in the Mauna Loa CGR, VEGAS

220 and CarbonTracker in the 2015/16 El Niño (Fig. 2d). In June 2016, the F_{TA} anomaly of

221 VEGAS and CarbonTracker reduced significantly (the sign changed), whereas the

222 Mauna Loa CGR reduced only slightly (no sign change; Fig. 2d). A similar

223 phenomenon also occurred earlier, from April to July 2015. In addition, the anomalous

224 carbon release caused by the El Niño lasted from approximately July in the El Niño

225 developing year to October in the El Niño decaying year (Figs. 2b–d). For simplicity,

226 we calculated the total anomalies of all El Niño events during this period in the next

227 context, taking the terrestrial lagged responses into account (Wang et al., 2016).

228 Based on the major geographical regions, we separated global F_{TA} anomaly into the

229 extratropical northern hemisphere (23°N–90°N), tropical regions (23°S–23°N), and

230 extratropical southern hemisphere (60°S–23°S). Because the F_{TA} anomaly over the

231 extratropical southern hemisphere is generally smaller, we mainly present the

232 evolutions of the F_{TA} over the extratropical northern hemisphere and the tropical regions

233 in Fig. 3. Comparing the global and tropical F_{TA} anomalies, the F_{TA} anomalies in the

234 tropical regions dominated the global F_{TA} during these El Niño events (Figs. 3b, d and

235 f), in accordance with previous conclusions (Peylin et al., 2013; Zeng et al., 2005). The

236 F_{TA} anomalies over the extratropical northern hemisphere were nearly neutral in

237 VEGAS for the composite and the 1997/98 El Niño events (Figs. 3a and c). However,

238 there was clear anomalous uptake from April to September in 2016 simulated by

239 VEGAS (Fig. 3e), compensating for the carbon release over the tropics (Fig. 3f). This

240 anomalous uptake caused the globally negative F_{TA} anomalies that occurred from May

241 to September in 2016 (Fig. 2d). Similar anomalous uptake also occurred over the

242 extratropical northern hemisphere from April to July 2015. This anomalous uptake in

243 VEGAS was to some extent consistent with the results from CarbonTracker, and

244 accounted for the global F_{TA} reduction mentioned above during these periods.

245 Comparing the behaviors between the Mauna Loa CGR and the F_{TA} anomalies, the

246 Mauna Loa CGR, which originates from a tropical observatory, does not reflect the

247 signals over the extratropical northern hemisphere in time (Figs. 2d and 3e).

248 Because F_{TA} mainly stems from the difference between TER and GPP, we present the

249 TER and GPP anomalies in Fig. 4 to clearly explain the F_{TA} anomalies. Anomalously

250 negative GPP dominated the F_{TA} anomaly in the tropics in the composite and the

251 1997/98 El Niño episodes, with the significant lagged responses (peak at approximately

252 May of the El Niño decaying year; Figs. 4b and d). Furthermore, clear positive TER

253 anomalies occurred from October 1997 to April 1998 (Fig. 4d), contributing to the

254 tropical carbon release during this period (Fig. 3d). In contrast, anomalously positive

255 TER dominated the F_{TA} anomaly in the tropics during the 2015/16 El Niño, without

256 clear lags (Fig. 4f), accounting for the disappearance of the terrestrial F_{TA} lagged

257 response (Fig. 2d). In the extratropical northern hemisphere, the increased GPP and

258 TER from April to October were nearly identical in the composite and in 1998 (Figs.

259 4a and c), causing neutral F_{TA} anomalies (Figs. 3a and c). However, the increased GPP

260 was stronger than the increased TER from April to July 2015 and from April to

261 September 2016 (Fig. 4e), resulting in the anomalous uptake in F_{TA} (Figs. 2d and 3e).

262 We calculated the total carbon flux anomalies from July in the El Niño developing year

263 to October in the El Niño decaying year. The composite global F_{TA} anomaly during the

264 El Niño events in VEGAS was approximately 0.60 Pg C yr^{-1}, dominated by tropical

265 ecosystems with 0.61 Pg C yr^{-1} (Table 2). These anomalies were comparable to the

266 mean of the CAMS and MACC inversion results, at 0.92$\pm$0.01 globally and 0.66$\pm$0.03

267 Pg C yr^{-1} in the tropics. In these two extreme cases, a strong anomalous carbon release

268 occurred during the 1997/98 El Niño, with a value of 1.64 Pg C yr^{-1}, which was less

269 than the 2.57 Pg C yr^{-1} in the CAMS and MACC inversions; while only 0.73 Pg C yr^{-1}

270 was released during the 2015/16 El Niño, which was comparable to the 0.82 Pg C yr^{-1}

271 in CarbonTracker. However, the F_{TA} anomalies in the tropical regions dominated the

272 global F_{TA} anomalies in both cases, with values of 1.70 and 1.12 Pg C yr^{-1} in VEGAS,

273 respectively. Furthermore, anomalous carbon uptake simulated by VEGAS over the

274 extratropical northern hemisphere cancelled out the 0.52 Pg C yr^{-1} anomalous release

275 in the tropics during the 2015/16 El Niño, whereas it was neutral (-0.05 Pg C yr^{-1}) in

276 the 1997/98 El Niño. The F_{TA} anomaly was relatively smaller in the extratropical

277   southern hemisphere.

278   In terms of the biological processes, the GPP (-0.73 Pg C yr^{-1}) and TER (0.62 Pg C

279   yr^{-1}) in the tropics together drove the anomalous F_{TA} during 1997/98, while the TER

280   (0.95 Pg C yr^{-1}) mainly drove the anomalous F_{TA} during 2015/16, with a near neutral

281   GPP of -0.03 Pg C yr^{-1} (Table 2). These data confirmed that the GPP played a more

282   important role in the 1997/98 event, while TER was dominant during the 2015/16 El

283   Niño. In the extratropical northern hemisphere, GPP and TER cancelled each other out.

284   They were 0.13 and 0.08 Pg C yr^{-1} in the composite analysis, and 0.63 and 0.55 Pg C

285   yr^{-1} in the 1997/98 El Niño, respectively, causing the near neutral F_{TA} anomaly in that

286   region. However, the GPP and TER in the 2015/16 El Niño were much stronger than

287   those in the composite or the 1997/98 El Niño. Importantly, the GPP (1.90 Pg C yr^{-1})

288   was stronger than the TER (1.45 Pg C yr^{-1}) in the 2015/16 El Niño, causing the

289   significant carbon uptake. The F_{TA} anomaly caused by wildfires also played an

290   important role during the 1997/98 El Niño, with a global value of 0.42 Pg C yr^{-1} in

291   VEGAS, which was consistent with the GFED fire data product (0.82 Pg C yr^{-1}). The

292   effect of wildfires on the F_{TA} anomaly during the 1997/98 El Niño episode has been

293   previously suggested by van der Werf et al. (2004), whereas it was close to zero (0.05

294   Pg C yr^{-1}) during the 2015/16 El Niño.

295

296   **3.2 Spatial features and its mechanisms**

297   The regional responses of terrestrial ecosystems to El Niño events are inhomogeneous,

298   principally due to the anomalies in climate variability. In the composite El Niño analysis

299   (Fig. 5a), land consistently released carbon flux in the tropics, while there was an

300   anomalous carbon uptake over the North America as well as the central and eastern

301   Europe. These regional responses were generally consistent with the CAMS and

302 MACC inversion results (Fig. 5d).

303 During the 1997/98 El Niño episode, the tropical responses were analogous to the

304 composite results, except for stronger carbon releases. North America and central and

305 eastern China had stronger carbon uptake, whereas Europe and Russia had stronger

306 carbon release (Fig. 5b). However, during the 2015/16 El Niño, anomalous carbon

307 uptake occurred over the Sahel and East Africa, compensating for the carbon release

308 over the other tropical regions (Fig. 5c). This made the total F_{TA} anomaly in the tropics

309 in 2015/16 less than that in 1997/98 (Figs. 3d and f; and Table 2). North America had

310 anomalous carbon uptake, similar to that in the composite and the 1997/98 El Niño,

311 while central and eastern Russia had anomalous carbon uptake during the 2015/16 El

312 Niño (Fig. 5c), which was opposite to the carbon release in the composite and the

313 1997/98 El Niño. This opposite behavior of the boreal forests over the central and

314 eastern Russia clearly contributed to the total uptake over the extratropical northern

315 hemisphere (Table 2). Moreover, these regional responses during the 2015/16 El Niño

316 were significantly consistent with the CarbonTracker result (Fig. 5f).

317 To better explain these regional carbon flux anomalies, we present the main climate

318 variabilities of soil wetness (mainly caused by precipitation) and air temperature, and

319 the biological processes of GPP and TER in Fig. 6. In the composite analyses, the soil

320 wetness is generally reduced in the tropics (Fig. 6a), causing the widespread decrease

321 in GPP (Fig. 6b), which has been verified by model sensitivity experiments (Qian et al.,

322 2008). At the same time, air temperature was anomalously warmer, contributing to the

323 increase in TER. However, the drier conditions in the semi-arid regions, such as the

324 Sahel, South Africa, and Australia, restricted this increase in TER induced by warmer

325 temperatures (Fig. 6d). Higher air temperatures over the North America largely

326 enhanced the GPP and TER, while cooler conditions over the Eurasia reduced them

327 (Figs. 6b–d). Wetter conditions over parts of North America and Eurasia also increased

328 the GPP and TER to some extent (Fig. 6a).

329 Comparing the composite results (Figs. 6a–d) and the 1997/98 El Niño (Figs.6e–h), the

330 regional patterns were almost identical, except for the difference in magnitude. In

331 contrast, there were some differences in the 2015/16 El Niño. Over the Sahel and East

332 Africa, the soil wetness increased due to the higher precipitation (Fig. 6i), dynamically

333 cooling the air temperature (Fig. 6k). These wetter conditions largely benefit GPP (Fig.

334 6j), compensating for the reduced GPP over the other tropical regions. This caused GPP

335 near neutral in the tropics, as compared to the composite and the 1997/98 El Niño (Table

336 2). Higher soil moisture also contributed to increased TER over the Sahel (Fig. 6l),

337 contrary to that in the 1997/98 El Niño (Fig. 6h). This spatial compensation in GPP,

338 together with the widespread increase in TER, accounted for the TER dominance in the

339 tropics during the 2015/16 El Niño. Furthermore, the higher GPP resulted in the

340 anomalous carbon uptake in that region (Fig. 5c), which partly compensated for the

341 anomalous carbon release over the other tropical regions. This in part caused the smaller

342 tropical F_{TA} during the 2015/16 El Niño compared with that during 1997/98. Another

343 clear difference occurred over the Eurasia, with almost opposite signals during the

344 1997/98 and 2015/16 El Niño events. During the 2015/16 El Niño over the Eurasia, air

345 temperature was anomalously higher compared with the cooling in the composite and

346 during the 1997/98 El Niño (Figs. 6c, g, and k). This warmth enhanced the GPP and

347 TER (Figs. 6j and l), as compared with the reduced levels in the composite and during

348 the 1997/98 El Niño (Figs. 6b, d, f, and h). This phenomenon explains the stronger GPP

349 and TER anomalies, and the anomalous carbon uptake over the whole of the

350 extratropical northern hemisphere (Table 2).

351 Recently, more attention has been paid to SIF as an effective indicator of GPP (Guanter

352   et al., 2014). Therefore, we compared the simulated GPP and SIF variabilities on the

353   interannual time scale. Although noisy signals in SIF occurred, it was anomalously

354   positive over the USA, parts of Europe, and East Africa, and negative over the Amazon

355   and South Asia, during the 2015/16 El Niño, corresponding to increased and decreased

356   GPP, respectively (Figs. 7a and c). The match over other regions was not significant. In

357   addition, MODIS EVI increased anomalously over the North America, southern South

358   America, parts of Europe, the Sahel, and East Africa, but reduced over the Amazon,

359   northern Canada, central Africa, South Asia, and northern Australia (Fig. 7d). These

360   EVI anomalies corresponded well with the simulated LAI anomalies (Fig. 7b). The

361   good match between the simulated GPP (LAI) and SIF (EVI) gives us more confidence

362   in the VEGAS simulations.

363   Finally, wildfires, as important disturbances for F_{TA}, always release carbon flux.

364   Although the F_{TA} anomalies caused by wildfires were generally smaller than the GPP

365   or TER anomalies, they played an important role during the 1997/98 El Niño (globally,

366   0.42 Pg C yr^{-1} in VEGAS and 0.82 Pg C yr^{-1} in GFED; Table 2), which is consistent

367   with previous work (van der Werf et al., 2004). The F_{TA} anomalies caused by wildfires

368   are shown in Fig. 8. The correlation coefficients between the simulated global F_{TA}

369   anomalies caused by wildfires and the GFED fire data product was 0.46 (unsmoothed)

370   and 0.63 (smoothed; Fig. 8a), confirming that VEGAS has certain capability in

371   simulating this disturbance. During the 1997/98 El Niño, satellite-based GFED data

372   show that the F_{TA} anomalies caused by wildfires mainly occurred over the tropical

373   regions, such as the Amazon, central Africa, South Asia, and Indonesia (Fig. 8d).

374   VEGAS also simulated the positive F_{TA} over these tropical regions (Fig. 8b). The total

375   tropical F_{TA} anomalies caused by fires were 0.37 Pg C yr^{-1} in VEGAS and 0.72 Pg C

376   yr^{-1} in GFED (Table 2). During the 2015/16 El Niño, wildfires also resulted in positive

377   F_{TA} anomalies over the Amazon, South Asia, and Indonesia; however, their magnitudes

378   were smaller than those during the 1997/98 El Niño, because it was much drier during

379   the 1997/98 event than the 2015/16 one (Figs. 6e and i). In addition, the wetter

380   conditions over East Africa during the 2015/16 El Niño suppressed the occurrences of

381   wildfires with the negative F_{TA} anomalies (Fig. 8c). The total tropical F_{TA} anomaly was

382   0.11 Pg C yr^{-1} in VEGAS (Table 2). Therefore, wildfires played a less important role

383   during the 2015/16 event than during the 1997-98 one. The F_{TA} anomalies caused by

384   wildfires over the extratropics were much weaker than those over the tropics, and the

385   match between VEGAS and GFED was poorer (Table 2; Figs. 8b and d).

386

387   **4   Conclusions and Discussion**

388   The magnitudes and patterns of climate anomalies caused by different El Niño events

389   differ. Therefore, the responses of terrestrial carbon cycle to different El Niño episodes

390   remain uncertain (Schwalm, 2011). In this study, we compared in detail the impacts of

391   two extreme El Niño events in recorded history (namely, the recent 2015/16, and earlier

392   1997/98 events) on the terrestrial carbon cycle in the context of a multi-event

393   'composite' El Niño. We used VEGAS in its near-real-time framework, along with

394   inversion datasets. The main conclusions can be summarized as follows:

395   (1) The simulations indicated that the global-scale F_{TA} anomaly during the 2015/16 El

396   Niño was 0.73 Pg C yr^{-1}, which was nearly two times smaller than that during the

397   1997/98 El Niño (1.64 Pg C yr^{-1}), and was confirmed by the inversion results. The

398   F_{TA} had no obvious lagged response during the 2015/16 El Niño, in contrast to that

399   during the 1997/98 El Niño. Separating the global fluxes, the fluxes in the tropics

400   and the extratropical northern hemisphere were 1.12 and -0.52 Pg C yr^{-1} during

401   the 2015/16 El Niño, respectively, whereas they were 1.70 and -0.05 Pg C yr^{-1}

402   during the 1997/98 event. Tropical F_{TA} anomalies dominated the global F_{TA}

403   anomalies during both extreme El Niño events.

404   (2) Mechanistic analysis indicates that anomalously wet conditions occurred over the

405   Sahel and East Africa during the 2015/16 El Niño, resulting in the increase in GPP,

406   which compensated for the reduction in GPP over the other tropical regions. In total,

407   this caused a near neutral GPP in the tropics (-0.03 Pg C yr^{-1}), compared with the

408   composite analysis (-0.54 Pg C yr^{-1}) and the 1997/98 El Niño (-0.73 Pg C yr^{-1}).

409   The spatial compensation in GPP and the widespread increase in TER (0.95 Pg C

410   yr^{-1}) explained the dominance of TER during the 2015/16 El Niño, compared with

411   the GPP dominance during the 1997/98 event. The different biological dominance

412   accounted for the phase difference in the F_{TA} responses during the 1997/98 and

413   2015/16 El Niño events.

414   (3) Higher air temperatures over North America largely enhanced the GPP and TER

415   during the 1997/98 and 2015-16 El Niño events. However, the air temperatures

416   during the 2015/16 El Niño over the Eurasia were anomalously higher, compared

417   with the cooling during the 1997/98 El Niño episode. These warmer conditions

418   benefited the GPP and TER, accounting for the stronger GPP (1.90 Pg C yr^{-1}) and

419   TER (1.45 Pg C yr^{-1}) anomalies and anomalous carbon uptake (-0.52 Pg C yr^{-1})

420   over the extratropical northern hemisphere during the 2015/16 El Niño.

421   (4) Wildfires, frequent in the tropics, played an important role in the F_{TA} anomalies

422   during the 1997/98 El Niño episode, confirmed by the VEGAS simulation and the

423   satellite-based GFED fire product. However, the VEGAS simulation showed that

424   the tropical F_{TA} caused by wildfires during the 2015/16 El Niño was relatively

425   smaller than that during the 1997/98 El Niño. This result was mainly because the

426   tropical weather was much drier during the 1997/98 event than during the 2015-16

427   one.

428   It is important to keep in mind that the responses of the terrestrial carbon cycle to the

429   El Niño events in this study were simulated using an individual DGVM (VEGAS),

430   which, whilst highly consistent with the variations in the CGR and inversion results,

431   carries uncertainties in terms of the regional responses because of, for example, its

432   model structure, biological processes considered, and parameterizations. Of course,

433   uncertainties exist in all of the state-of-the-art DGVMs. Fang et al. (2017) recently

434   suggested that none of the 10 contemporary terrestrial biosphere models captures the

435   ENSO-phase-dependent responses. If possible, we will quantify the inter-model

436   uncertainties in regional responses of the terrestrial carbon cycle to El Niño events

437   when the new round of TRENDY simulations (1901–2016) becomes available.

438   Although we used three inversion datasets as reference for the VEGAS simulation in

439   this study, they cover different periods. Importantly, there are also large uncertainties

440   between the different atmospheric CO_2 inversions because of their different prescribed

441   priors, *a priori* uncertainties, inverse methods, and observational datasets (Peylin et al.,

442   2013). Future atmospheric CO_2 inversions may produce more accurate results based on

443   more observational datasets, including surface and satellite-based observations.

444   Recently, more studies have pointed out that the 1997/98 El Niño evolved following

445   the eastern Pacific El Niño dynamics, which depends on basin-wide thermocline

446   variations, whereas the 2015/16 event involves additionally the central Pacific El Niño

447   dynamics that relies on the subtropical forcing (Paek et al., 2017; Palmeiro et al., 2017).

448   Therefore, it is necessary to investigate the different impacts of the eastern and central

449   Pacific El Niño types (Ashok et al., 2007) on the terrestrial carbon cycle in the future.

450   This may give us an additional insight into the contrasting responses of the terrestrial

451   carbon cycle to the 1997/98 and 2015/16 El Niño events. We believe that doing so will

452   contribute greatly to deepening our knowledge of present and future carbon cycle

453   variations on the interannual time scales.

454

455   **Data Availability**

456   In this study, all the datasets can be freely accessed. The Mauna Loa monthly CO_2

457   records are available at https://www.esrl.noaa.gov/gmd/ccgg/trends/data.html. The

458   ERSST4 Niño3.4 index can be accessed from

459   http://www.cpc.ncep.noaa.gov/data/indices/ersst4.nino.mth.81-10.ascii. The CAMS

460   and MACC inversions are available at http://apps.ecmwf.int/datasets/. The

461   CarbonTracker datasets can be found at

462   https://www.esrl.noaa.gov/gmd/ccgg/carbontracker/. The GFEDv4 global fire

463   emissions are downloaded at https://daac.ornl.gov/cgi-bin/dsviewer.pl?ds_id=1293.

464   Satellite SIF datasets are retrieved from

465   http://avdc.gsfc.nasa.gov/pub/data/satellite/MetOp/GOME_F/MetOp-A/level3/.

466   MODIS enhanced vegetation index (EVI) datasets are downloaded from

467   https://lpdaac.usgs.gov/dataset_discovery/modis/modis_products_table/mod13c2_v00

468   6.

469

470   **Acknowledgements:**

471   We gratefully acknowledge the ESRL for the use of their Mauna Loa atmospheric CO_2

472   records and CarbonTracker datasets; NOAA for the ERSST4 ENSO index; LSCE-IPSL

473   for the CAMS and MACC inversion datasets; the Oak Ridge National Laboratory

474   Distributed Active Archive Center for the GFEDv4 global fire emissions; NASA

475   Goddard Space Flight Center for the SIF datasets; and the Land Processes Distributed

476   Active Archive Center for the MODIS EVI datasets. This study was supported by the

National Key R&D Program of China (Grant No. 2016YFA0600204 and No. 2017YFB0504000) and the Natural Science Foundation for Young Scientists of Jiangsu Province, China (Grant No. BK20160625).

References

Ahlstrom, A., Raupach, M. R., Schurgers, G., Smith, B., Arneth, A., Jung, M., Reichstein, M., Canadell, J. G., Friedlingstein, P., Jain, A. K., Kato, E., Poulter, B., Sitch, S., Stocker, B. D., Viovy, N., Wang, Y. P., Wiltshire, A., Zaehle, S., and Zeng, N.: The dominant role of semi-arid ecosystems in the trend and variability of the land CO_2 sink, Science, 348, 895-899, 2015.

Anderegg, W. R., Ballantyne, A. P., Smith, W. K., Majkut, J., Rabin, S., Beaulieu, C., Birdsey, R., Dunne, J. P., Houghton, R. A., Myneni, R. B., Pan, Y., Sarmiento, J. L., Serota, N., Shevliakova, E., Tans, P., and Pacala, S. W.: Tropical nighttime warming as a dominant driver of variability in the terrestrial carbon sink, Proc Natl Acad Sci U S A, 112, 15591-15596, 2015.

Ashok, K., Behera, S. K., Rao, S. A., Weng, H., and Yamagata, T.: El Niño Modoki and its possible teleconnection, J. Geophys. Res., 112, C11007, 2007.

Bacastow, R. B.: Modulation of atmospheric carbon dioxide by the Southern Oscillation, Nature, 261, 116-118, 1976.

Bousquet, P., Peylin, P., Ciais, P., Le Quere, C., Friedlingstein, P., and Tans, P. P.: Regional changes in carbon dioxide fluxes of land and oceans since 1980, Science, 290, 1342-1346, 2000.

Capotondi, A., Wittenberg, A. T., Newman, M., Lorenzo, E. Di, Yu, J. Y., Braconnot, P., Cole, J., Dewitte, B., Giese, B., Guilyardi, E., Jin, F. F., Karnauskas, K., Kirtman, B., Lee, T., Schneider, N., Xue, Y., and Yeh, S. W.: Understanding ENSO diversity,

Bulletin of the American Meterological Society, 96, 921-938, 2015.

Chen, M., Xie, P., Janowiak, J. E., and Arkin, P. A.: Global Land Precipitation: A 50-yr Monthly Analysis Based on Gauge Observations, Journal of Hydrometeorology, 3, 249-266, 2002.

Chevallier, F.: On the parallelization of atmospheric inversions of CO_2 surface fluxes within a variational framework, Geosci Model Dev, 6, 783-790, 2013.

Clark, D. A., Piper, S. C., Keeling, C. D., and Clark, D. B.: Tropical rain forest tree growth and atmospheric carbon dynamics linked to internnual tempreature variation during 1984-2000, P. Natl. Acad. Sci. USA, 100, 5852-5857, 2003.

Cox, P. M., Pearson, D., Booth, B. B., Friedlingstein, P., Huntingford, C., Jones, C. D., and Luke, C. M.: Sensitivity of tropical carbon to climate change constrained by carbon dioxide variability, Nature, 494, 341-344, 2013.

Didan, K.: MOD13C2 MODIS/Terra Vegetation Indices Monthly L3 Global 0.05Deg CMG V006. NASA EOSDIS Land Processes DAAC. https://doi.org/10.5067/MODIS/MOD13C2.006, 2015.

Doughty, C. E., and Goulden, M. L.: Are tropical forests near a high temperature threshold?, J. Geophys. Res., 113, G00B07, 2008.

Fang, Y., Michalak, A. M., Schwalm, C. R., Huntzinger, D. N., Berry, J. A., Ciais, P., Piao, S. L., Poulter, B., Fisher, J. B., Cook, R. B., Hayes, D., Huang, M. Y., Ito, A., Jain, A., Lei, H. M., Lu, C. Q., Mao, J. F., Parazoo, N. C., Peng, S. S., Ricciuto, D. M., Shi, X. Y., Tao, B., Tian, H. Q., Wang, W. L., Wei, Y. X., and Yang, J.: Global land carbon sink response to temperature and precipitation varies with ENSO phase, Environ. Res. Lett., 12, 064007, 2017.

Friedlingstein, P., Cox, P., Betts, R., Bopp, L., Von Bloh, W., Brovkin, V., Cadule, P., Doney, S., Eby, M., Fung, I., Bala, G., John, J., Jones, C., Joos, F., Kato, T., Kawamiya,

527   M., Knorr, W., Lindsay, K., Matthews, H. D., Raddatz, T., Rayner, P., Reick, C.,

528   Roeckner, E., Schnitzler, K. G., Schnur, R., Strassmann, K., Weaver, A. J., Yoshikawa,

529   C., and Zeng, N.: Climate-carbon cycle feedback analysis: Results from the C^{4}MIP

530   model intercomparison, Journal of Climate, 19, 3337-3353, 2006.

531   Guanter, L., Zhang, Y. G., Jung, M., Joiner, J., Voigt, M., Berry, J. A., Frankenberg, C.,

532   Huete, A. R., Zarco-Tejada, P., Lee, J. E., Moran, M. S., Ponce-Campos, G., Beer, C.,

533   Camps-Valls, G., Buchmann, N., Gianelle, D., Klumpp, K., Cescatti, A., Baker, J. M.,

534   and Griffis, T. J.: Global and time-resolved monitoring of crop photosynthesis with

535   chlorophyll fluorescence, PNAS, doi: 0.1073/pnas.1320008111, 2014. E1327–E1333,

536   2014.

537   Hansen, J., Ruedy, R., Sato, M., and Lo, K.: Global Surface Temperature Change,

538   Reviews of Geophysics, 48, 2010.

539   Huang, B., Banzon, V. F., Freeman, E., Lawrimore, J., Liu, W., Peterson, T. C., Smith,

540   T. M., Thorne, P. W., Woodruff, S. D., and Zhang, H.-M.: Extended Reconstructed Sea

541   Surface Temperature Version 4 (ERSST.v4). Part I: Upgrades and Intercomparisons,

542   Journal of Climate, 28, 911-930, 2015.

543   Huntzinger, D. N., Schwalm, C., Michalak, A. M., Schaefer, K., King, A. W., Wei, Y.,

544   Jacobson, A., Liu, S., Cook, R. B., Post, W. M., Berthier, G., Hayes, D., Huang, M., Ito,

545   A., Lei, H., Lu, C., Mao, J., Peng, C. H., Peng, S., Poulter, B., Riccuito, D., Shi, X.,

546   Tian, H., Wang, W., Zeng, N., Zhao, F., and Zhu, Q.: The North American Carbon

547   Program Multi-Scale Synthesis and Terrestrial Model Intercomparison Project – Part 1:

548   Overview and experimental design, Geosci Model Dev, 6, 2121-2133, 2013.

549   Janowiak, J. E. and Xie, P.: CAMS-OPI: A Global Satellite-Rain Gauge Merged

550   Product for Real-Time Precipitation Monitoring Applications, J. Clim., 12, 3335-3342,

551   1999.

Joiner, J., Yoshida, Y., Vasilkov, A. P., Middleton, E. M., Campbell, P. K. E., Yoshida, Y., Kuze, A., and Corp, L. A.: Filling-in of near-infrared solar lines by terrestrial fluorescence and other geophysical effects: simulations and space-based observations from SCIAMACHY and GOSAT, Atmospheric Measurement Techniques, 5, 809-829, 2012.

Jung, M., Reichstein, M., Margolis, H. A., Cescatti, A., Richardson, A. D., Arain, M. A., Arneth, A., Bernhofer, C., Bonal, D., Chen, J. Q., Gianelle, D., Gobron, N., Kiely, G., Kutsch, W., Lasslop, G., Law, B. E., Lindroth, A., Merbold, L., Montagnani, L., Moors, E. J., Papale, D., Sottocornola, M., Vaccari, F., and Williams, C.: Global patterns of land-atmosphere fluxes of carbon dioxide, latent heat, and sensible heat derived from eddy covariance, satellite, and meteorological observations, J Geophys Res-Biogeo, 116, 2011.

Jung, M., Reichstein, M., Schwalm, C. R., Huntingford, C., Sitch, S., Ahlstrom, A., Arneth, A., Camps-Valls, G., Ciais, P., Friedlingstein, P., Gans, F., Ichii, K., Jain, A. K., Kato, E., Papale, D., Poulter, B., Raduly, B., Rodenbeck, C., Tramontana, G., Viovy, N., Wang, Y. P., Weber, U., Zaehle, S., and Zeng, N.: Compensatory water effects link yearly global land CO_2 sink changes to temperature, Nature, 541, 516-520, 2017.

Keeling, C. D., Bacastow, R. B., Bainbridge, A. E., Ekdahl, C. A., Guenther, P. R., Waterman, L. S., and Chin, J. F. S.: Atmospheric Carbon-Dioxide Variations at Mauna-Loa Observatory, Hawaii, Tellus, 28, 538-551, 1976.

Keeling, C. D., Whorf, T. P., Wahlen, M., and Vanderplicht, J.: Interannual Extremes in the Rate of Rise of Atmospheric Carbon-Dioxide since 1980, Nature, 375, 666-670, 1995.

Kim, J. S., Kug, J. S., Yoon, J. H., and Jeong, S. J.: Increased atmospheric CO2 growth rate during El Niño driven by reduced terrestrial productivity in the CMIP5 ESMs,

577   Journal of Climate, 29, 8783-8805, 2016.

578   Klein Goldewijk, K., Beusen, A., Van Drecht, G., and De Vos, M.: The HYDE 3.1

579   spatially explicit database of human-induced global land-use change over the past

580   12,000 years, Global Ecology and Biogeography, 20, 73-86, 2011.

581   Mercado, L. M., Bellouin, N., Sitch, S., Boucher, O., Huntingford, C., Wild, M., and

582   Cox, P. M.: Impact of changes in diffuse radiation on the global land carbon sink, Nature,

583   458, 1014-U1087, 2009.

584   Paek, H., Yu, J.-Y., and Qian, C.: Why were the 2015/16 and 1997/1998 extreme El

585   Niño different?, Geophys. Res. Lett., 44, 18848-1856, 2017.

586   Palmeiro, F. M., Iza, M., Barriopedro, D., Calvo, N., and Garcia-Herrera, R.: The

587   complex behavior of El Niño winter 2015-2016, Geophys. Res. Lett., 44, 2902-2910,

588   2017.

589   Peters, W., Jacobson, A. R., Sweeney, C., Andrews, A. E., Conway, T. J., Masarie, K.,

590   Miller, J. B., Bruhwiler, L. M., Petron, G., Hirsch, A. I., Worthy, D. E., van der Werf,

591   G. R., Randerson, J. T., Wennberg, P. O., Krol, M. C., and Tans, P. P.: An atmospheric

592   perspective on North American carbon dioxide exchange: CarbonTracker, Proc Natl

593   Acad Sci U S A, 104, 18925-18930, 2007.

594   Peylin, P., Law, R. M., Gurney, K. R., Chevallier, F., Jacobson, A. R., Maki, T., Niwa,

595   Y., Patra, P. K., Peters, W., Rayner, P. J., Rödenbeck, C., van der Laan-Luijkx, I. T., and

596   Zhang, X.: Global atmospheric carbon budget: results from an ensemble of atmospheric

597   CO_2 inversions, Biogeosciences, 10, 6699-6720, 2013.

598   Piao, S., Sitch, S., Ciais, P., Friedlingstein, P., Peylin, P., Wang, X., Ahlström, A., Anav,

599   A., Canadell, J. G., Cong, N., Huntingford, C., Jung, M., Levis, S., Levy, P. E., Li, J.,

600   Lin, X., Lomas, M. R., Lu, M., Luo, Y., Ma, Y., Myneni, R. B., Poulter, B., Sun, Z.,

601   Wang, T., Viovy, N., Zaehle, S., and Zeng, N.: Evaluation of terrestrial carbon cycle

models for their response to climate variability and to CO_2 trends, Global Change

Biology, doi: 10.1111/gcb.12187, 2013. 2117–2132, 2013.

Qian, H., Joseph, R., and Zeng, N.: Response of the terrestrial carbon cycle to the El

Nino-Southern Oscillation, Tellus Series B-Chemical and Physical Meteorology, 60,

537-550, 2008.

Randerson, J. T., van der Werf, G. R., Giglio, L., Collatz, G. J. and Kasibhatla, P.

S.:Global Fire Emissions Database, Version 4, (GFEDv4). ORNL DAAC, Oak Ridge,

Tennessee, USA. http://dx.doi.org/10.3334/ORNLDAAC/1293, 2015.

Schwalm, C. R.: Does terrestrial drought explain global CO_2 flux anomalies induced

by El Nino?, Biogeosciences, 8, 2493-2506, 2011.

Sitch, S., Friedlingstein, P., Gruber, N., Jones, S. D., Murray-Tortarolo, G., Ahlström,

A., Doney, S. C., Graven, H., Heinze, C., Huntingford, C., Levis, S., Levy, P. E., Lomas,

M., Poulter, B., Viovy, N., Zaehle, S., Zeng, N., Arneth, A., Bonan, G., Bopp, L.,

Canadell, J. G., Chevallier, F., Ciais, P., Ellis, R., Gloor, M., Peylin, P., Piao, S. L., Le

Quéré, C., Smith, B., Zhu, Z., and Myneni, R.: Recent trends and drivers of regional

sources and sinks of carbon dioxide, Biogeosciences, 12, 653-679, 2015.Tian, H. Q.,

Melillo, J. M., Kicklighter, D. W., McGuire, A. D., Helfrich, J. V. K., Moore, B., and

Vorosmarty, C. J.: Effect of interannual climate variability on carbon storage in

Amazonian ecosystems, Nature, 396, 664-667, 1998.

University of East Anglia Climatic Research Unit, Harris, I.C., Jones, P.D.: CRU

TS3.22: Climatic Research Unit (CRU) Time-Series (TS) Version 3.22 of High

Resolution Gridded Data of Month-by-month Variation in Climate (Jan. 1901- Dec.

2013). NCAS British Atmospheric Data Centre, 2014.

van der Werf, G. R., Randerson, J. T., Collatz, G. J., Giglio, L., Kasibhatla, P. S.,

Arellano, A. F., Jr., Olsen, S. C., and Kasischke, E. S.: Continental-scale partitioning of

627   fire emissions during the 1997 to 2001 El Nino/La Nina period, Science, 303, 73-76,

628   2004.

629   Wang, J., Zeng, N., and Wang, M.: Interannual variability of the atmospheric CO_2

630   growth rate: roles of precipitation and temperature, Biogeosciences, 13, 2339-2352,

631   2016.

632   Wang, W., Ciais, P., Nemani, R., Canadell, J. G., Piao, S., Sitch, S., White, M. A.,

633   Hashimoto, H., Milesi, C., and Myneni, R. B.: Variations in atmospheric CO_2 growth

634   rates coupled with tropical temperature, PNAS, 110, 13061-13066, 2013.

635   Wang, X., Piao, S., Ciais, P., Friedlingstein, P., Myneni, R. B., Cox, P., Heimann, M.,

636   Miller, J., Peng, S., Wang, T., Yang, H., and Chen, A.: A two-fold increase of carbon

637   cycle sensitivity to tropical temperature variations, Nature, 506, 212-215, 2014.

638   Wei, Y., Liu, S., Huntzinger, D. N., Michalak, A. M., Viovy, N., Post, W. M., Schwalm,

639   C. R., Schaefer, K., Jacobson, A. R., Lu, C., Tian, H., Ricciuto, D. M., Cook, R. B.,

640   Mao, J., and Shi, X.: The North American Carbon Program Multi-scale Synthesis and

641   Terrestrial Model Intercomparison Project – Part 2: Environmental driver data, Geosci

642   Model Dev, 7, 2875-2893, 2014.

643   Zeng, N., Mariotti, A., and Wetzel, P.: Terrestrial mechanisms of interannual CO_2

644   variability, Global Biogeochemical Cycles, 19, GB1016, 2005.

645   Zeng, N., Qian, H. F., Munoz, E., and Iacono, R.: How strong is carbon cycle-climate

646   feedback under global warming?, Geophys Res Lett, 31, 2004.

647   Zeng, N., Zhao, F., Collatz, G. J., Kalnay, E., Salawitch, R. J., West, T. O., and Guanter,

648   L.: Agricultural Green Revolution as a driver of increasing atmospheric CO_2 seasonal

649   amplitude, Nature, 515, 394-397, 2014.

650

651

652

653

654

655

Tables and Figures:

Table 1 Lists of El Niño events from 1980 till 2016.

No.	El Niño Events	Duration (months)	Maximum Nino3.4 Index (°C)
1	Apr1982–Jun1983	15	2.1
2	Sep1986–Feb1988	18	1.6
3	Jun1991–Jul1992	14	1.6
4	Oct1994–Mar1995	6	1.0
5	May1997–May1998	13	2.3
6	Jun2002–Feb2003	9	1.2
7	Jul2004–Apr2005	10	0.7
8	Sep2006–Jan2007	5	0.9
9	Jul2009–Apr2010	10	1.3
10	Nov2014–May2016	19	2.3

658

659 **Table 2** Carbon flux anomalies during El Niño events, calculated as the mean from July

660 in the El Niño developing year to October in the El Niño decaying year. Flux units are

661 in Pg C yr^{-1}.

		Inversions		VEGAS Model				GFED
Zones	El Niños	F_{TA} (CAMS+MACC)[a]	F_{TA} (CarbonTracker)	F_{TA}	GPP	TER	C_{fire}	C_{fire}
Global	composite[b]	0.92±0.01	–	0.60	−0.55	−0.08	0.14	–

	1997/98	2.57±0.04	–	1.64	−0.04	1.28	0.42	0.82
	2015/16	–	0.82	0.73	1.59	2.24	0.05	–
NH	composite	0.20±0.02	–	−0.06	0.13	0.08	−0.01	–
	1997/98	0.40±0.07	–	−0.05	0.63	0.55	0.04	0.11
	2015/16	–	0.18	−0.52	1.90	1.45	−0.06	–
Tropical	composite	0.66±0.03	–	0.61	−0.54	−0.07	0.15	–
	1997/98	2.12±0.14	–	1.70	−0.73	0.62	0.37	0.72
	2015/16	–	0.53	1.12	−0.03	0.95	0.11	–
SH	composite	0.07±0.01	–	0.05	−0.14	−0.09	0.00	–
	1997/98	0.05±0.02	–	−0.02	0.14	0.12	0.00	−0.01
	2015/16	–	0.11	0.14	−0.28	−0.16	0.00	–

[a]represents the mean value of the CAMS and MACC inversion results with the uncertainty of their standard deviation.

[b]Composite analyses exclude the 1982/83, 1991/92, and 2015/16 El Niño events, because the former two cases were disturbed by the El Chichón and Pinatubo eruptions, and the latter is not covered by the inversion datasets.

668
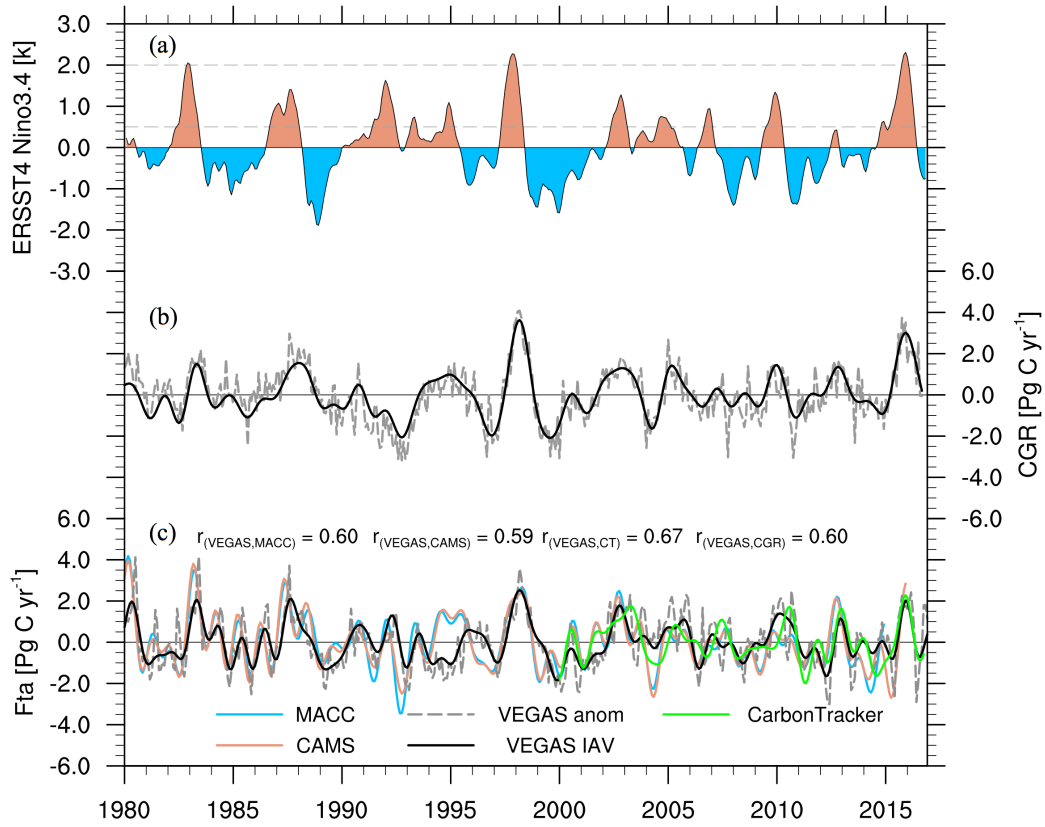
Figure 1. Interannual variability (IAV) in the sea surface temperature anomaly (SSTA)

and carbon cycle. (a) ERSST4 Niño3.4 Index (units: K) using the 3-month running

averaged SSTA for the Niño 3.4 region (5°N–5°S, 120°–170°W). (b) IAV in the Mauna

Loa CO_2 growth rate (CGR; units: Pg C yr^{-1}). The CGR is calculated as the difference

between the monthly mean in adjacent years. The dashed line is the detrended monthly

anomaly and the solid line is smoothed by the butterworth filtering. (c) IAV in the land–

atmosphere carbon fluxes (F_{TA}; units: Pg C yr^{-1}). The blue and orange solid lines are

the smoothed results of the MACC and CAMS inversions, respectively. The gray

dashed line is the detrended anomaly and the black one is the smoothed result from the

VEGAS model simulation. The green solid line is the smoothed CarbonTracker result.

679
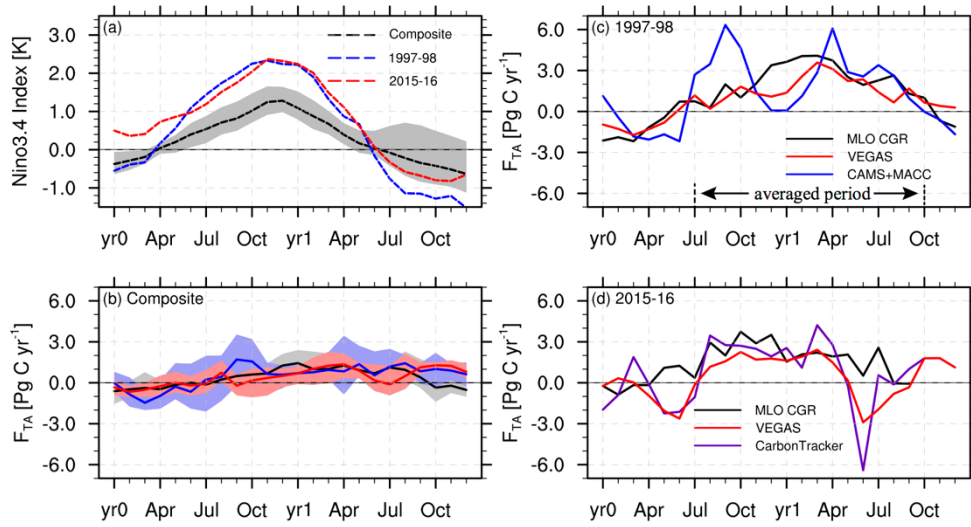
Figure 2. Evolutions of the global F_{TA} along with the development of El Niño. (a) the SSTA in the composite (black), 1997/98 (blue), and 2015/16 (red) El Niño events. (b) The F_{TA} anomalies in the El Niño composite analysis. The black solid line denotes the Mauna Loa CGR; and the red and blue lines show the VEGAS and mean of the CAMS and MACC inversions, respectively. The shaded areas in (a) and (b) show the 95% confidence intervals of the variables in the composite, derived in 1000 bootstrap estimates. (c) The F_{TA} anomalies during the 1997/98 El Niño events. The arrows demonstrate the time periods during which we calculate the carbon flux anomalies listed/presented in the table and figures. (d) The F_{TA} anomalies during the 2015/16 El Niño. The purple line denotes the result of the CarbonTracker2016 and CarbonTracker near-real-time datasets.

693
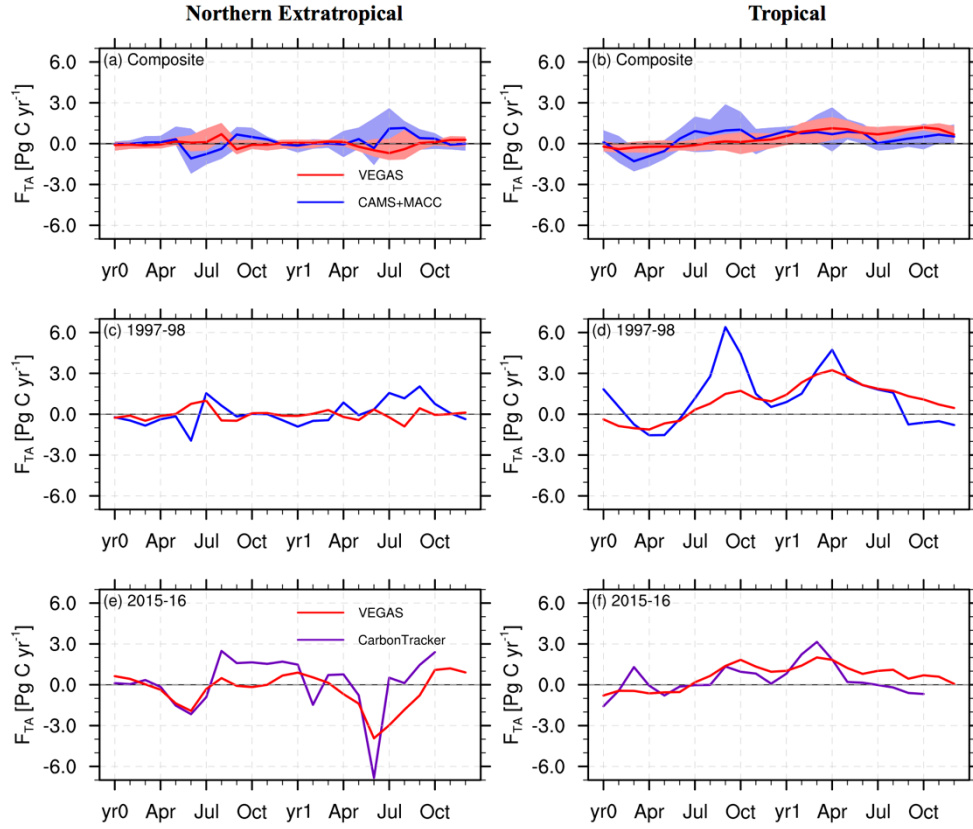
694   **Figure 3**. Evolutions of F_{TA} over the extratropical northern hemisphere (23°N–90°N)

695   and tropical regions (23°S–23°N) along with the development of El Niño. (a, b)

696   Composite results with the VEGAS simulation (red solid line) and the mean of the

697   CAMS and MACC inversions (blue solid line). The shaded areas show the 95%

698   confidence intervals of the variables in the composite, derived in 1000 bootstrap

699   estimates. (c, d) The F_{TA} anomalies during the 1997/98 El Niño. (e, f) The F_{TA}

700   anomalies in the 2015/16 El Niño with VEGAS (red solid line) and CarbonTracker

701   (purple solid line).

702

703
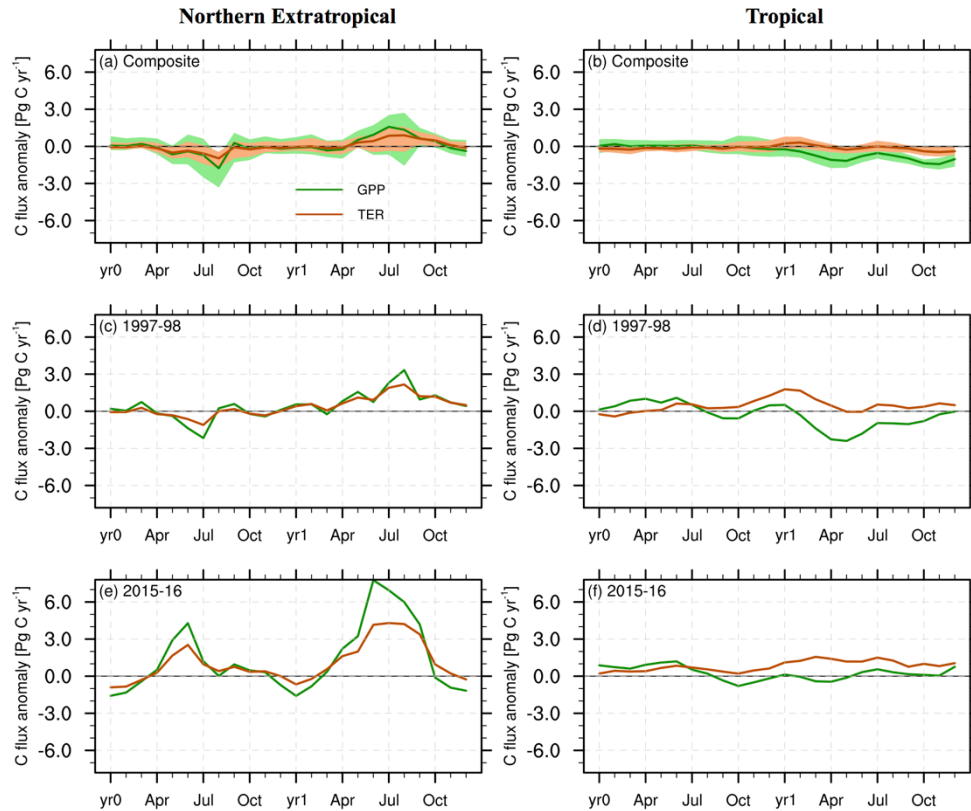
Figure 4. Evolutions of gross primary productivity (GPP, green lines) and terrestrial ecosystem respiration (TER, brown lines) over the extratropical northern hemisphere (23°N–90°N) and tropical regions (23°S–23°N) along with the development of El Niño. (a, b) El Niño composite results. The shaded areas show the 95% confidence intervals of the variables in the composite, derived in 1000 bootstrap estimates. (c, d) Results of the 1997/98 El Niño. (e, f) Results of the 2015/16 El Niño.

710

711
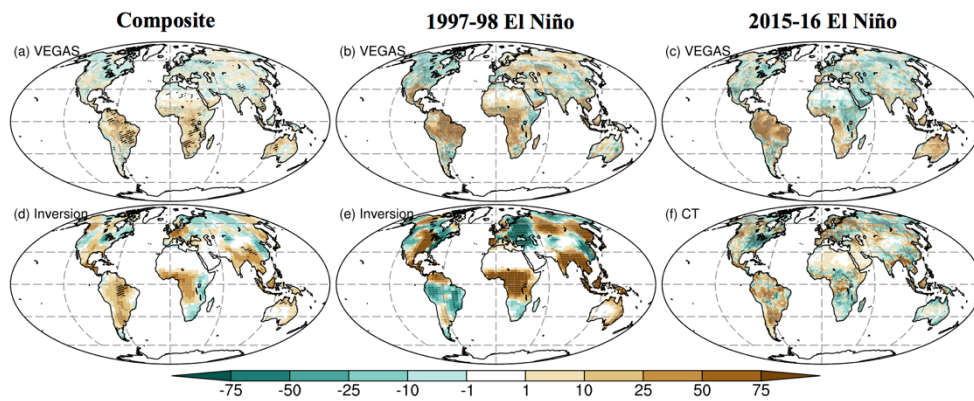
Figure 5. Spatial F_{TA} anomalies calculated from July in the El Niño developing year to October in the El Niño decaying year (units: g C m^{-2} yr^{-1}). (a–c) Results of the composite, 1997/98, and 2015/16 El Niño events simulated by VEGAS, respectively. (d–e) The averaged results of CAMS and MACC in the composite and 1997/98 El Niños. (f) The 2015/16 El Niño F_{TA} anomaly in CarbonTracker. The stippled areas in (a) and (d) are significant above the 90% level, estimated by Student's *t*-test.

718

719

720

Composite

1997-98 El Nino

2015-16 El Nino

721
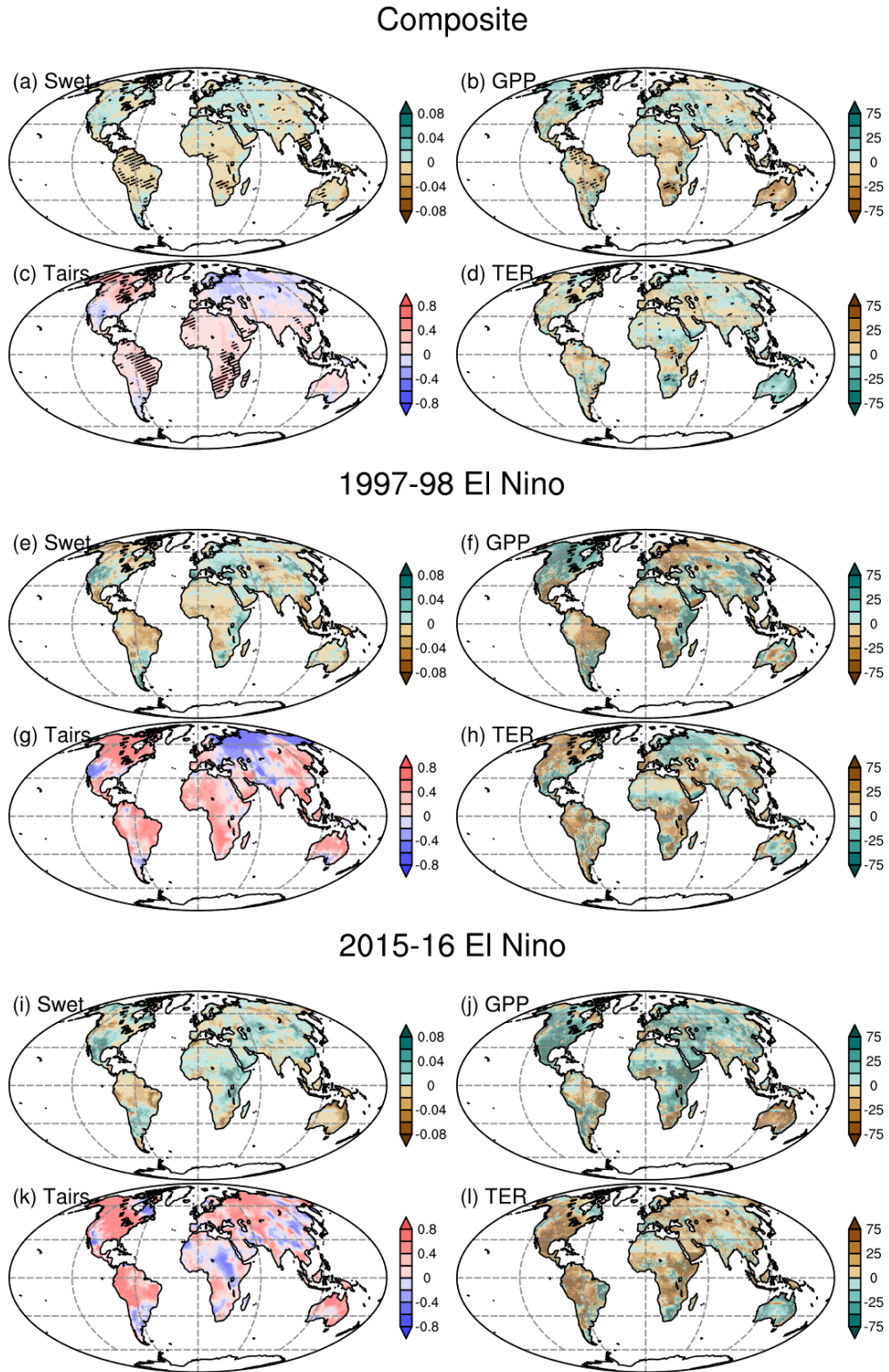
Figure 6. Anomalies of soil wetness, air temperature (units: K), GPP (g C m^{-2} yr^{-1}),

and TER (g C m^{-2} yr^{-1}) from July in the El Niño developing year to October in the El

Niño decaying year in the composite, 1997/98, and 2015/16 El Niño episodes,

725   respectively. (a–d) Results of the composite analyses. The stippled areas are significant

726   above the 90% levels estimated by the Student's *t*-test. (e–h) Anomalies during the

727   1997/98 El Niño. (i–l) Anomalies during the 2015/16 El Niño.

728

729
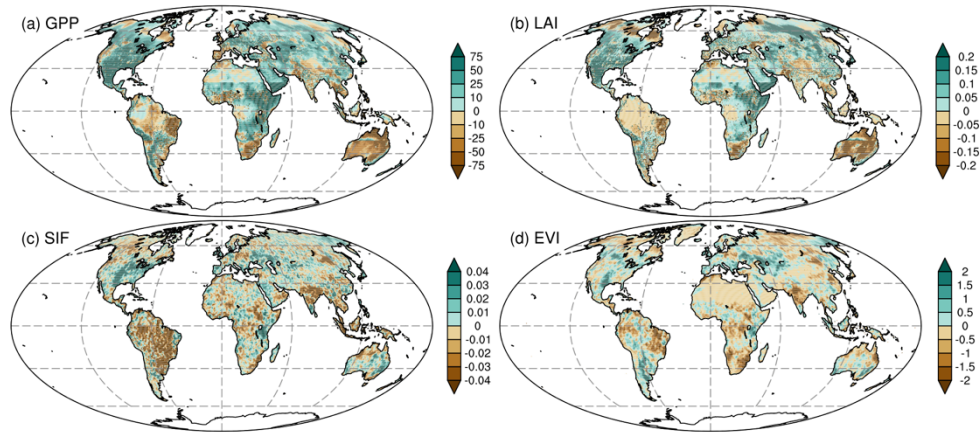
730   **Figure 7.** Spatial anomalies in (a) the simulated GPP by VEGAS (units: g C m^{-2} yr^{-1}),

731   (b) the simulated leaf area index (LAI, units: m^2 m^{-2}), (c) solar-induced chlorophyll

732   fluorescence (SIF, units: mW m^{-2} nm^{-1} sr^{-1}), and (d) MODIS enhanced vegetation

733   index (EVI, $\times 10^{-2}$) from July 2015 to October 2016.

734

735
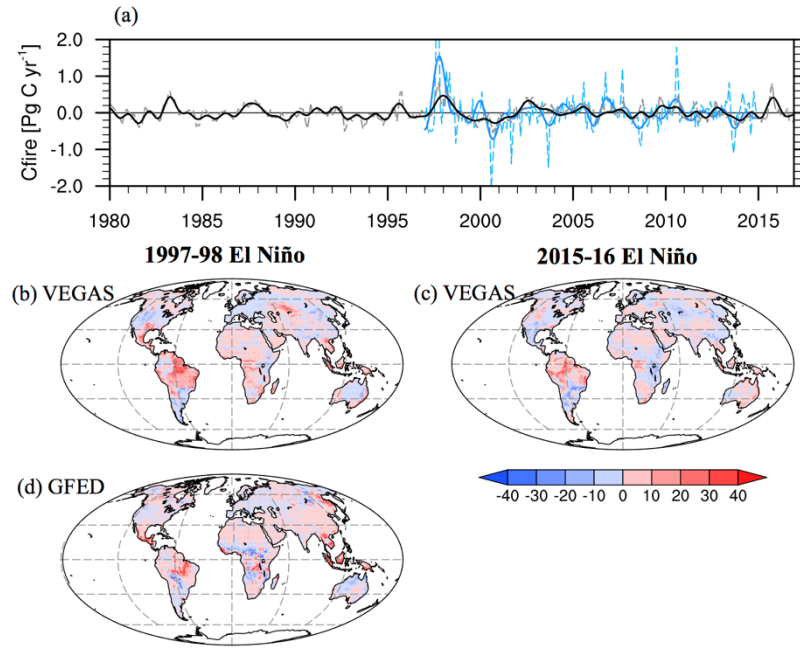
736 **Figure 8.** F_{TA} anomalies induced by wildfires. (a) Total global anomalies (Pg C yr^{-1}).

737 The dashed gray and solid black lines represent the anomalies simulated by VEGAS,

738 detrended and smoothed by Butterworth filtering, respectively. The dashed and solid

739 blue lines represent the GFED results. (b) Spatial F_{TA} anomaly (g C m^{-2} yr^{-1}) during

740 the 1997/98 El Niño in VEGAS. (c) Spatial F_{TA} anomaly during the 2015/16 El Niño

741 in VEGAS. (d) GFED anomaly during the 1997/98 El Niño episode.

742

743